Supplemental material for "What controls thermo-osmosis? Molecular simulations show the critical role of interfacial hydrodynamics"

Li Fu,[1] Samy Merabia,[1] and Laurent Joly[1,*]

[1] *Univ Lyon, Université Claude Bernard Lyon 1, CNRS, Institut Lumière Matière, F-69622 Villeurbanne, France*

[*] laurent.joly@univ-lyon1.fr

CONTENTS

I. SIMULATION DETAILS

In this work, all simulations were performed with the LAMMPS package [S1]. The initial configurations were prepared using LAMMPS build-in tools for Lennard-Jones systems, and Moltemplate [S2] for water/graphene systems. The visualization was realized using VMD [S3]. In this section, the technical details of simulations on Lennard-Jones systems will be presented firstly, both through mechano-caloric and thermo-osmotic routes. The second part will be devoted to water/graphene systems using the mechano-caloric route.

A. Lennard-Jones systems

Generic liquid/solids (walls and pistons) systems were made of Lennard-Jones (LJ) particles in this part for both mechano-caloric and thermo-osmotic routes.

LJ reduced units were used with a set of characteristic parameters based on liquid particles: mass m, distance σ and energy ε in the liquid-liquid LJ interaction potential $V(r) = 4\varepsilon[(\sigma/r)^{12} - (\sigma/r)^6]$, with r the distance between the particles. Time and temperature are expressed in units of $\tau = (m\sigma^2/\varepsilon)^{1/2}$ and ε/k_B, respectively. A cut-off distance of 4.5σ was carefully chosen (See Section III). Solids were constructed by face-centered cubic (fcc) unit cells with a LJ reduced density of $1\sigma^{-3}$. A timestep of 0.005τ was used for all the simulations in this part.

"Einstein solids", in which particles are bound by harmonic springs to their equilibrium positions, were used to model the solid walls and pistons. Lindemann criterion of melting states that crystals melt when the average amplitude of thermal vibrations of atoms is relatively high compared with interatomic distances, e.g. $\sqrt{< a_c^2 >} \sim Ld_s$, where a_c is the critical amplitude of atomic thermal vibration at melting, $L \approx 0.10$ is the Lindemann parameter,and d_s is the nearest neighbor distance of solid atoms, which can be estimated as $2^{1/6}\sigma$ for a fcc solid with a reduced density of $1\sigma^{-3}$. Since all atoms are linked with a harmonic spring with spring constant K, their average thermal vibration energy in one direction can be estimated by:

$$E = \frac{1}{2}Ka^2 \sim \frac{1}{2}k_BT. \tag{S1}$$

According to Lindemann criterion, to prevent the melting of solid walls, the spring constant K should be larger than a critical value:

$$K \gg K_c \sim \frac{k_BT}{a_c^2}. \tag{S2}$$

With an average temperature of $0.85\varepsilon/k_B$, $K_c \sim 70\ \varepsilon/\sigma^2$. We took thus a value of $250\varepsilon/\sigma^2$ for K in our simulations.

1. Mechano-caloric route

As shown in Fig. S1a, this configuration consists of a simulation box with dimensions of $25.44 \times 25.44 \times 38.16\sigma^3$. An Einstein solid wall with a thickness of 3.18σ is at the

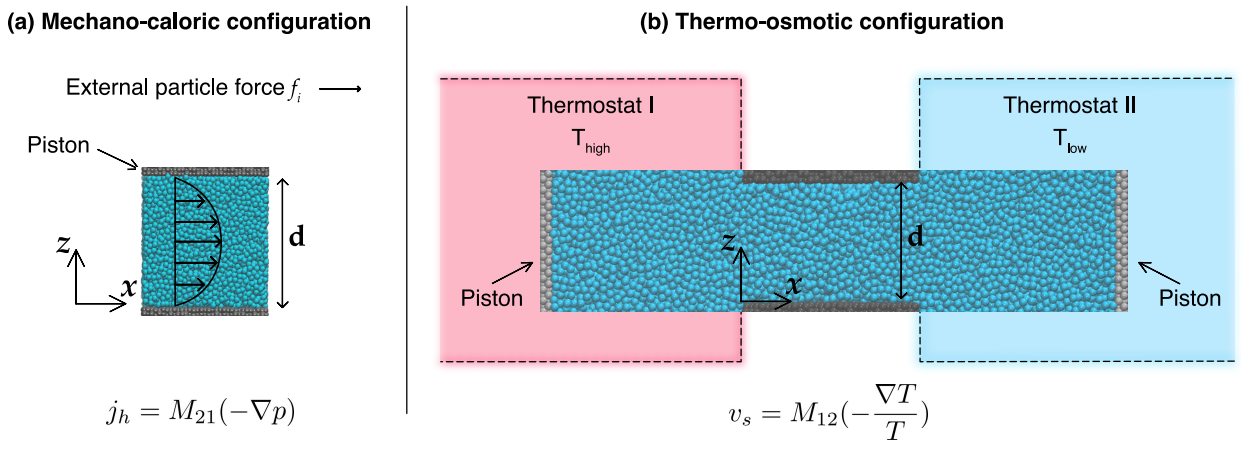

FIG. S1. Illustration of the different configurations used to measure the thermo-osmosis coefficient with molecular dynamics simulations. (a) Mechano-caloric route, using a slit nano-channel without reservoirs: a body force per particle f_i is applied to the liquid particles to model an external pressure gradient, and an excess heat flux is generated by the induced Poiseuille flow; (b) Thermo-osmotic route, where the nanochannel is connected to reservoirs at different temperatures and the thermo-osmotic velocity is measured.

bottom of the simulation box. A piston is set at the top and a pressure of $0.1\varepsilon/\sigma^3$ is applied on it in the $-z$ direction in order to enclose the liquid. The liquid and solids are thermostatted at $0.85\varepsilon/k_B$ with a canonical sampling thermostat that uses global velocity rescaling with Hamiltonian dynamics [S4]. We impose periodic boundary conditions in the x and y directions to construct an infinite slit nanochannel.

The system is firstly equilibrated for 50,000 MD steps, then an external particle force f_i is applied on liquid particles in the x direction to generate a Poiseuille flow in the channel. The pressure gradient can be computed as $-\nabla p = f_V = f_i N/V$ where f_V is the external volume force, N is the total number of liquid particles in the slit and V is the slit volume. After another 50,000 steps, the production run begins and the velocity profile is recorded and smoothed over 5,000,000 steps. All the hydrodynamic velocity profiles are found to be parabolic. The viscosity η as well as the slip length b can be thus extracted from the fitting curves using the following function [S5]:

$$v(z) = \frac{-\nabla p}{2\eta}[db + (z - z_s)(d - z + z_s)], \tag{S3}$$

where d is the slit gap; z_s is the thickness of immobile layers, which can be measured directly

from the profiles at the position where the velocity vanishes. The local specific enthalpy was expressed as

$$h(z) = (u_i(z) + p_i(z))\rho(z), \tag{S4}$$

where $u_i(z) = \frac{1}{2}mv_i^2 + \sum \phi_{ij}$ is the internal energy per particle (sum of the kinetic and potential energies), $p_i(z)$ is the atom-based virial expression for pressure, and $\rho(z)$ is the density profile. In particular, the term $p_i(z)$ is computed via:

$$p_i(z) = -(\mathbb{S}_{xx} + \mathbb{S}_{yy} + \mathbb{S}_{zz})/3, \tag{S5}$$

where $\mathbb{S}_{ab}$ is the *negative* of the ab component of the symmetric per-atom stress tensor, computed directly in LAMMPS via the `compute stress/atom` command [S6]. Note that it is indeed a stress per atom $\times$ atomic volume formulation, meaning the computed quantity is in units of pressure $\times$ volume (energy). The profiles of enthalpy were recorded to compute M_{12} (see main text).

2. Thermo-osmotic route

In the thermo-osmotic configuration, we use a nanochannel (slit gap 17.5 σ) connected to two reservoirs filled with liquid (see Fig. S1b). The two reservoirs are thermostatted independently with a canonical sampling thermostat that uses global velocity rescaling with Hamiltonian dynamics [S4]. The dimension of solid walls is identical to that used in the mechano-caloric configuration ($25.44 \times 25.44 \times 3.18\sigma^3$). Each reservoir has a length of 31.8σ in the x direction in the initial state. Two pistons are added at the extremities of the simulation box, and a pressure of $0.1\varepsilon/\sigma^3$ is applied on each piston in order to enclose the liquid. Periodic boundary conditions are imposed in the y and z directions.

Similarly to the mechano-caloric route, the system is firstly equilibrated for 50,000 MD steps, thermostatting both the liquid and solids at the same temperature T_{middle}. A ramp of temperature in the reservoirs is then realized by increasing the temperature of thermostat 1 to T_{high} and decreasing the temperature of thermostat 2 to T_{low}. After another 100,000 steps for stabilization, the production period begins and the temperatures of the two thermostats are kept constant. The sets of temperatures for producing temperature gradients in the nanochannel are presented in table I.

TABLE I. Sets of temperatures used to produce temperature gradients in the nanochannel (in units of ε/k_B).

	Set 1	Set 2	Set 3
T_{high}	1.0	0.95	0.9
T_{middle}	0.85	0.85	0.85
T_{low}	0.7	0.75	0.8

Besides the enthalpy profiles, the evolution of particle numbers in each reservoir is equally recorded, which will be used to calculate the flow velocity (see Section II).

B. Water-graphene system

In order to avoid hydrodynamic entrance effects, we performed simulations on a water-graphene system using the mechano-caloric route. The geometric configuration is very similar to that with the LJ model (see Fig.S2a). The simulation box consists of two graphene sheets and 2304 water molecules in between. The graphene sheet is constructed from rectangular unit cells containing 4 carbon atoms. The length of the long side of this rectangular cell is $a_1 = 3d$ and that of the short side is $a_2 = \sqrt{3}d$, where $d = 1.42\,\text{Å}$ is the distance between carbon atoms. We consider a graphene sheet with $\sim 38\,\text{Å}$ in length and $\sim 39\,\text{Å}$ in width at the bottom of the simulation box. The center of this graphene sheet is fixed at its initial position via a harmonic spring, and the solid is thermostatted at 323 K. Another graphene piston with the same size is applied at the top of the simulation box and a pressure of 1 atmosphere is applied homogeneously on it in the $-z$ direction. The movement of the piston in the other two directions is prohibited. The initial gap width between these sheets is $\sim 56\,\text{Å}$.

We used the TIP4P/2005 force field for water [S7], the LCBOP one for graphene [S8] and a recently proposed force field for water-carbon interactions [S9], which has been shown to reproduce accurately quantum chemistry calculations of interaction energies between water and carbon nanostructures [S10]. For all simulations with this system, we used a cutoff radius for LJ interaction of $12\,\text{Å}$ and a real-space Coulomb cutoff radius of $10\,\text{Å}$ for the purpose of computational efficiency. Long-range Coulombic interactions were computed using the

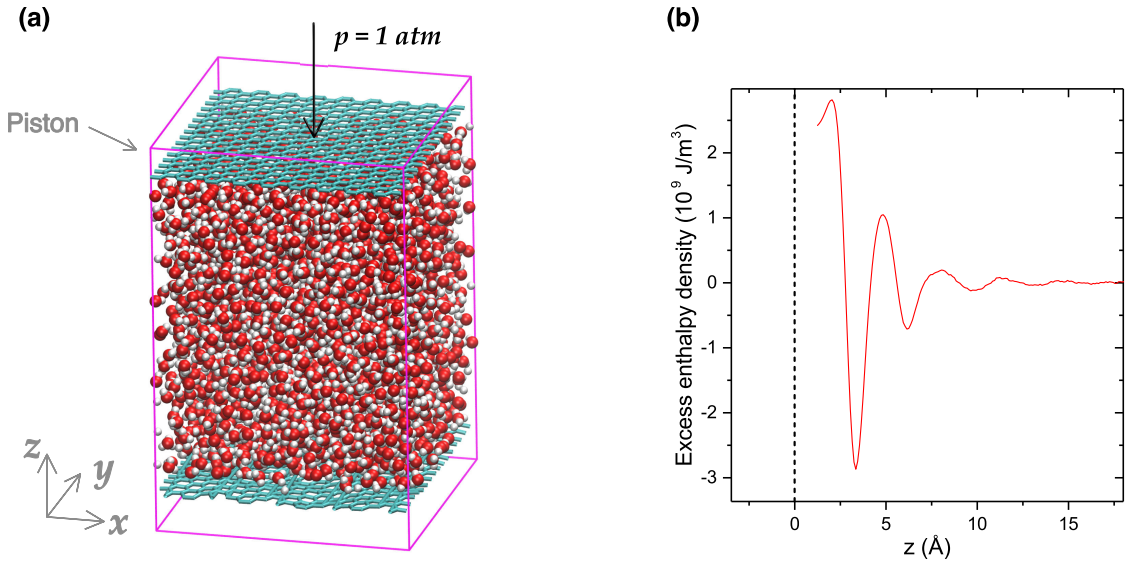

FIG. S2. (a)Illustration of the water-graphene system, using the mechano-caloric route. (b)Excess specific enthalpy profile for the water-graphene system. The graphene sheet is at the position $z = 0$.

particle-particle particle-mesh (PPPM) method, and water molecules were held rigid using the SHAKE algorithm.

Water molecules were firstly equilibrated at a constant temperature of 323 K for 50 ps. We then applied an external force F_{ext} on the liquid particles in the x direction, and the order of magnitude of F_{ext} is discussed below. After a relaxation time of 2 ns, the production period was held for 7.5 ns for each simulation. We ran five independent simulations from distinct initial configurations to reduce statistical uncertainties. Fig. S2b shows an example of the excess enthalpy density profile for this system.

To determine the order of magnitude of F_{ext}, since at 323 K, the average thermal velocity of water molecules in the x direction is about 380 m/s, the force induced hydrodynamic velocity should be largely inferior to this value. On the other hand, it is known that the water-graphene system presents a very weak interfacial friction and the time to attain the steady state of hydrodynamic flow could be long. The hydrodynamic velocity should also not be too small otherwise any perturbation at the beginning of simulations can delay substantially the steady state. We considered that 20 m/s could be a good choice. The external force F_{ext} was then calculated by $F_{\text{ext}} = 2\lambda A v_x$, where λ is the liquid-solid friction coefficient which is well documented for water-graphene system, and A is the area of the

graphene sheet. All these result in an external force F_{ext} of about 0.8×10^{-11} N.

II. THERMO-OSMOTIC ROUTE AND UNCERTAINTY EVALUATION

In the thermo-osmotic configuration, the unidirectional temperature gradient induced flow can be described by the following formula:

$$v_s = M_{12}\left(-\frac{\nabla T}{T}\right), \tag{S6}$$

where v_s is the flow velocity, M_{12} is the thermo-osmotic transport coefficient, ∇T is the temperature gradient and T is the average temperature. A positive M_{12} leads to a liquid flow towards the cold side, whereas a negative M_{12} drives the liquid towards the hot side.

The thermo-osmotic velocity v_s can be deduced from the definition of the volumetric flow rate:

$$Q = \frac{\Delta N/\rho}{\Delta t} = v_s S, \tag{S7}$$

with $S = L_y L_z$ the surface of the section and ρ the liquid number density. This leads to

$$v_s = \frac{\Delta N}{\Delta t}\frac{L_x}{N}, \tag{S8}$$

where N is the total liquid particle number in the zone of interest.

Since we can accurately measure the temperature in the slit as well as the number density of liquid, the uncertainty for the thermo-osmosis coefficient estimation comes from the linear fitting of the curve of v_s against $-\nabla T/T$. For each value of ε_{ls}, we perform 6 independent measurements to plot the curve. The expanded uncertainty is then evaluated by:

$$\Delta x = ks = k\frac{\sigma_x}{\sqrt{n}}, \tag{S9}$$

where k is the coverage factor, s is the combined standard uncertainty, σ_x is the standard deviation of the slope of fitting line and n is the number of measurements. With a level of confidence of 95%, $k = 2.57$ for 6 measurements for each ε_{ls}.

III. CHOICE OF INTERACTION CUTOFF RADIUS FOR LJ SYSTEMS

In order to estimate the influence of r_c on the measurement of M, we performed tests for $\varepsilon_{ls} = 0.3$, with the same set of temperature as depicted in Table I. A traditional r_c is set

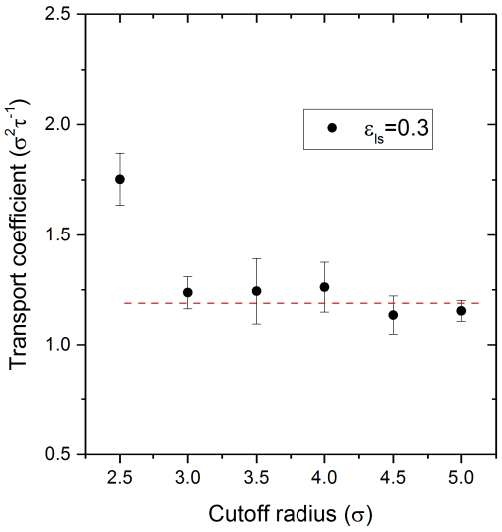

FIG. S3. Thermo-osmotic transport coefficient (in σ^2/τ) *vs* cutoff radius.

at 2.5σ for a computational efficiency, while larger r_c gives more accurate results. We used different r_c from 2.5σ to 5σ.

Figure S3 shows the evolution of M_{12} against the cutoff radius, measured using the thermo-osmosis route. Six independent measurements were realized for each point in the figure and the uncertainty is estimated as described in section II. Taking the error bars into account, we found that the results converge from $r_c = 3.0\sigma$.

On the other hand, the transport coefficient relies on the excess specific enthalpy δh, which is deduced from the excess atomic enthalpy δh_i (obtained from the atomic internal energy and the atom-based virial expression for pressure) and the number density profile (see Eq. S4). The influence of the cutoff radius on these parameters is consequently studied.

Figure S4 presents the evolution of the excess atomic enthalpy (δh_i) at the solid-liquid interface. We found that from $r_c = 3.5\sigma$, the curves begin to overlap, and that for $r_c = 4.5\sigma$ and $r_c = 5.0\sigma$ they are almost identical.

In Figures S5 and S6 the kinetic energy and potential energy profiles are plotted. Kinetic energy profiles show no difference for these cutoff radii, while the potential energy profiles for $r_c = 2.5\sigma$ and 3.0σ differ slightly from others.

Another important factor to the enthalpy determination is the stress tensor. In figures S7 and S8, the product of atomic normal pressure and atomic volume (virial expression of normal pressure $p_N V$) as well as that of atomic tangential pressure and atomic volume ($p_T V$) are plotted at the solid-liquid interface. Profiles for $r_c = 2.5$, 3.0 and 3.5σ are clearly

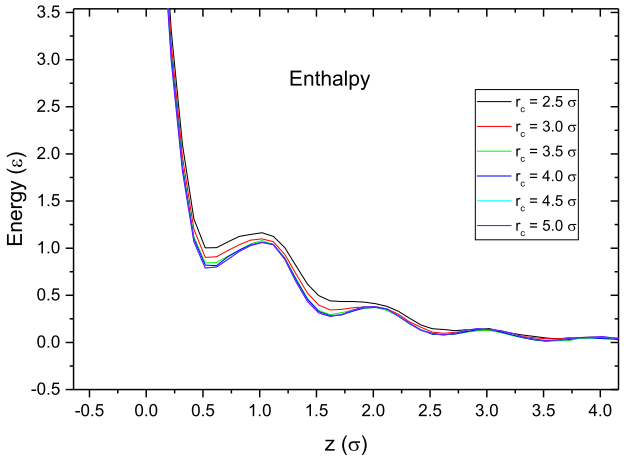

FIG. S4. Excess atomic enthalpy profiles at the solid-liquid interface with different cutoff radii.

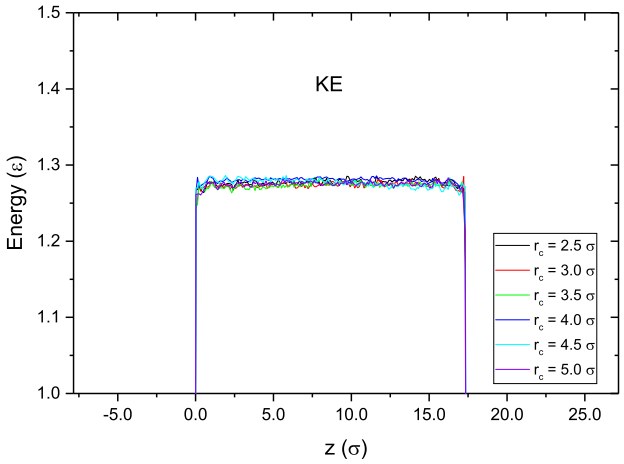

FIG. S5. Atomic kinetic energy profiles with different cutoff radii.

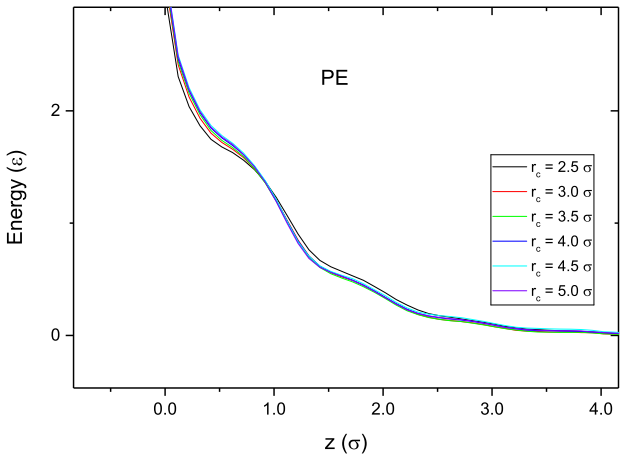

FIG. S6. Atomic potential energy profiles at the solid-liquid interface with different cutoff radii. The curves are shifted vertically so that they coincide in the bulk.

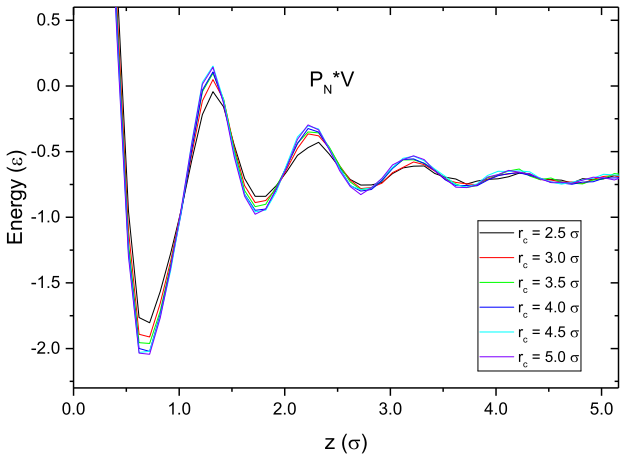

FIG. S7. $p_N V$ profiles (see text) at the solid-liquid interface with different cutoff radii.

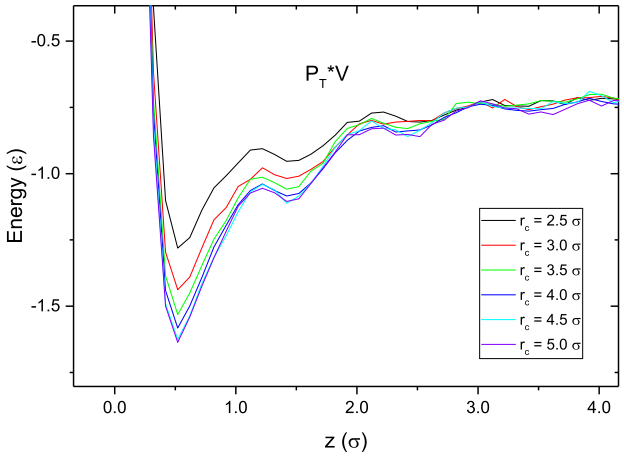

FIG. S8. $p_T V$ profiles (see text) profiles at the solid-liquid interface with different cutoff radii.

distinguished from others with higher r_c. Again, results for $r_c = 4.5\sigma$ and $r_c = 5.0\sigma$ are almost identical.

Another critical parameter which can be influenced by the cutoff radius is the density profile, which is used to deduce the specific enthalpy from the atomic enthalpy ($h = h_i \times \rho$). Figure S9 presents the density profiles at the interface, from which the cutoff radii of 4.0, 4.5 and 5.0σ give converged results. We can conclude that a cutoff radius of 4.0 σ is satisfying while using $r_c = 4.5\sigma$ is more reliable. Since the use of $r_c = 4.5\sigma$ is not computationally much more expensive than that of $r_c = 4.0\sigma$, we chose to work with $r_c = 4.5\sigma$ for the LJ model.

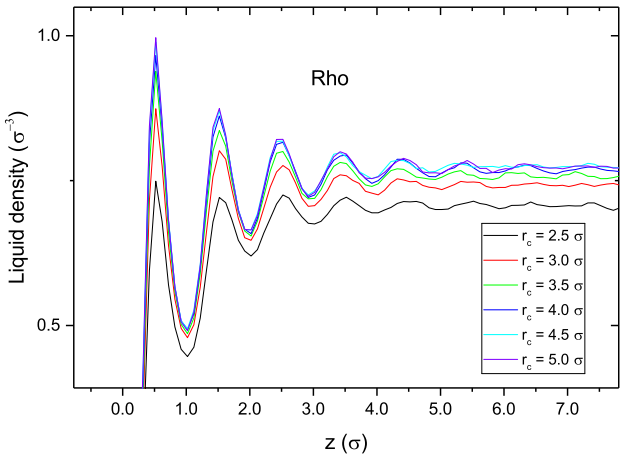

FIG. S9. Number density at the solid-liquid interface with different cutoff radii.

IV. DERIVATION OF AN EXPRESSION FOR THE THERMO-OSMOSIS COEFFICIENT

Using both the thermo-osmosis and the mechano-caloric configurations, we will here derive an expression for the thermo-osmosis coefficient accounting for the details of interfacial hydrodynamics, Eq. (3) of the main text. Specifically, we will assume a partial slip boundary condition with a slip length b applying at the shear plane position z_s (see velocity profile in Fig. S10.b):

$$v(z_\mathrm{s}) = b \left.\frac{\mathrm{d}v}{\mathrm{d}z}\right|_{z=z_\mathrm{s}}, \tag{S10}$$

with z the direction normal to the interface and $v(z)$ the velocity parallel to the interface. Note that Eq. (S10) can describe a no-slip boundary condition with a stagnant liquid layer ($b = 0$ and $z_\mathrm{s} > z_\mathrm{wall}$), or a slipping interface where there is generally no stagnant layer ($b \neq 0$ and $z_\mathrm{s} = z_\mathrm{wall}$).

A. Thermo-osmosis configuration

As discussed in Ref. [S11], the thermo-osmotic flow generated at a solid surface by a thermal gradient parallel to the interface can be obtained by solving Stokes equation with a thermodynamic force induced by the thermal gradient.

Indeed, the solid wall modifies the specific chemical potential μ in the liquid within an interaction length e. In the following we will refer to the layer of liquid affected by the

solid wall as the boundary layer, whose thickness is therefore e. Under a thermal gradient ∇T, the fluid experiences a thermodynamic force $T\nabla(\mu/T)$ in the boundary layer. Using the Gibbs-Helmholtz relation $\mathrm{d}(\mu/T)/\mathrm{d}T = -\delta h/T^2$, where δh is the local excess specific enthalpy in the fluid, one can re-express the thermodynamic force as: $\delta h(\nabla T/T)$. One can then solve Stokes equation:

$$-\eta\frac{\mathrm{d}^2 v}{\mathrm{d}z^2} = \delta h(z) \times \frac{\nabla T}{T}, \tag{S11}$$

with z the direction normal to the interface, $v(z)$ the velocity along the direction of the thermal gradient ∇T, η the shear viscosity of the liquid (assumed homogeneous), and $\delta h(z)$ the excess specific enthalpy profile in the liquid. Assuming a partial slip boundary condition with a slip length b applying at the shear plane z_s, one can compute the thermo-osmotic velocity in the bulk liquid $v_\mathrm{s} = v(z \gg e)$, and the corresponding response coefficient M:

$$M = \frac{v_\mathrm{s}}{-\nabla T/T} = \frac{1}{\eta}\int_{z_\mathrm{s}}^{z\gg e} (z - z_\mathrm{s} + b)\delta h(z)\,\mathrm{d}z. \tag{S12}$$

This expression and its derivation are very similar to the ones presented by Huang et al. [S12, S13] for the electro-osmosis response coefficient, except that the electrical force is replaced here by the thermodynamic force, and the charge density profile is replaced by the excess specific enthalpy profile.

Finally, the standard expression originally derived by Derjaguin, Eq. (2) of the main text, is retrieved for $z_\mathrm{s} = b = 0$.

B. Mechano-caloric configuration

One can also derive the expression for the thermo-osmosis coefficient in the reciprocal mechano-caloric configuration, where a pressure gradient creates a Poiseuille flow, which transports the interfacial excess enthalpy and thus generates a heat flux. The thermo-osmosis coefficient M relates the produced heat flux J_h to the applied pressure gradient ∇p:

$$\frac{J_h}{A} = M(-\nabla p), \tag{S13}$$

with A the cross-section of the channel.

Let's consider a channel of arbitrary cross-section $\mathcal{S}$ (see Fig. S10.a), and assume the thickness e of the boundary layer (with non-zero excess enthalpy) is much smaller than the typical size of the channel. The heat flux J_h originates from the convective transport

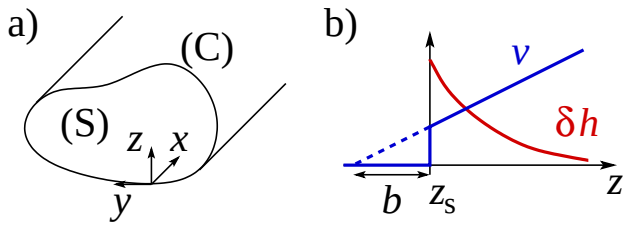

FIG. S10. a) Mechano-caloric heat flux in a channel of arbitrary cross-section $\mathcal{S}$, with a thin boundary layer (where the specific enthalpy differs from its bulk value). The heat flux J_h is the sum of infinitesimal heat fluxes $\mathrm{d}J_h$ generated at line elements $\mathrm{d}y$ of the contour $\mathcal{C}$ of the cross-section. These infinitesimal heat fluxes are the integrals along the local normal z to the contour, of the heat flux density $j_h = \delta h\, v$, with δh the excess specific enthalpy and v the liquid velocity along the x direction. b) schematic excess specific enthalpy and velocity profiles at a solid surface with a partial slip BC (slip length b) applying at the shear plane z_s. The velocity profile writes $v = \dot{\gamma}(z - z_\mathrm{s} + b)$ for $z > z_\mathrm{s}$, where $\dot{\gamma}$ is the local shear rate in the boundary layer.

of the excess enthalpy in the boundary layer, located along the contour $\mathcal{C}$ of the channel cross-section. Defining a local reference frame along the contour, with x the direction of the flow, y and z the local tangent and normal to the contour, respectively, J_h can therefore be expressed as the sum of the infinitesimal heat fluxes $\mathrm{d}J_h$ arising at line elements $\mathrm{d}y$ of the contour (Fig. S10.b):

$$J_h = \oint_{\mathcal{C}} \mathrm{d}J_h, \tag{S14}$$

with

$$\mathrm{d}J_h = \mathrm{d}y \int_{z_\mathrm{s}}^{z \gg e} \mathrm{d}z\ \delta h(z)\ v(z), \tag{S15}$$

where z is the local normal to the surface, z_s the position of the shear plane, δh the excess specific enthalpy and v the liquid velocity along the x direction. If e is much smaller than the channel size, the curved Poiseuille velocity profile can be approximated by a simple shear velocity profile over the extent of the boundary layer (with a partial slip boundary condition applying at the shear plane z_s): $v(z) = (z - z_\mathrm{s} + b)(\mathrm{d}v/\mathrm{d}z)|_{z=z_\mathrm{s}}$ (Fig. S10.b). The infinitesimal heat flux can then be written:

$$\mathrm{d}J_h = \mathrm{d}y \left.\frac{\mathrm{d}v}{\mathrm{d}z}\right|_{z=z_\mathrm{s}} \times \int_{z_s}^{z \gg e} \mathrm{d}z\, (z - z_s + b)\, \delta h(z), \tag{S16}$$

so that:

$$J_h = \oint_{\mathcal{C}} \mathrm{d}y \left.\frac{\mathrm{d}v}{\mathrm{d}z}\right|_{z=z_\mathrm{s}} \times \int_{z_s}^{z \gg e} \mathrm{d}z\, (z - z_s + b)\, \delta h(z). \tag{S17}$$

The second Green theorem can be used to transform the integral over the contour of the channel into an integral over the cross-section of the channel of the Laplacian of the velocity:

$$\oint_{\mathcal{C}} \mathrm{d}y \ \left.\frac{\mathrm{d}v}{\mathrm{d}z}\right|_{z=z_\mathrm{s}} = \iint_{\mathcal{S}} \mathrm{d}S \ \nabla^2 v. \tag{S18}$$

One can finally use Stokes equation, $\nabla^2 v = -\nabla p/\eta$ (assuming a homogeneous viscosity), to obtain an expression for the heat flux as a function of the pressure gradient,

$$J_h = A(-\nabla p/\eta) \times \int_{z_s}^{z \gg e} \mathrm{d}z \, (z - z_s + b) \, \delta h(z), \tag{S19}$$

and for the corresponding response coefficient:

$$M = \frac{1}{\eta} \int_{z_s}^{z \gg e} \mathrm{d}z \, (z - z_s + b) \, \delta h(z). \tag{S20}$$

This expression is identical to the one derived in the thermo-osmotic configuration, in line with Onsager reciprocal relations.

C. Large slip length limit

In Eq. (S12), only the region of the boundary layer (where $\delta h(z) \neq 0$) contributes to the integral. In this region $z - z_\mathrm{s}$ is at most on the order of the thickness e of the boundary layer. Therefore, if the slip length b is much larger than e, one can neglect $z - z_\mathrm{s}$ as compared to b where $\delta h(z) \neq 0$, and Eq. (S12) can be simplified:

$$M_{12} = M_{21} = \frac{b}{\eta} \int_{z_s}^{z \gg e} \delta h(z) \, \mathrm{d}z. \tag{S21}$$

Here we note that the partial slip boundary condition, Eq. (S10), physically stems from the identification of the viscous shear stress in the liquid close to the interface, $\eta \partial_z v$, and an interfacial friction stress proportional to the slip velocity, $\lambda \, v(z_\mathrm{s})$, defining the interfacial (fluid) friction coefficient λ [S14]. Accordingly, the slip length, bulk liquid viscosity and interfacial friction coefficient are related: $b = \eta/\lambda$, and in Eq. (S21) one can rewrite: $b/\eta = 1/\lambda$. Finally, in the large slip length limit there is no stagnant layer, so that the shear plane position identifies with the position of the solid wall: $z_\mathrm{s} = z_\mathrm{wall}$.

Therefore, when the slip length is large as compared to the thickness of the boundary layer, Eq. (S21) can be simplified as:

$$M = \frac{1}{\lambda} \int_{z_\mathrm{wall}}^{z \gg e} \delta h(z) \, \mathrm{d}z. \tag{S22}$$

The thermo-osmosis coefficient then depends only on the total interfacial enthalpy excess and on the liquid-solid friction coefficient.

This result can be retrieved with a simple argument: when $b \gg e$, the velocity profile is almost constant over the extent of the boundary layer, so that there is no shear in the liquid and the velocity jump is localized at the wall. The thermo-osmotic velocity then results from a simple force balance between the total thermodynamic force experienced by the boundary layer, $F/A = \int \delta h(\nabla T/T)$, and the interfacial friction force, $F'/A = -\lambda v_{\rm s}$. Writing that $F + F' = 0$ and using the definition of M, one obtains Eq. (S22).

V. CONTACT ANGLE IN LJ SYSTEMS

The wetting behavior of a liquid-solid interface is usually represented by the contact angle $0 \leq \theta \leq 180°$, which depends on the system temperature and the droplet size. The present work, however, has no intention to study in detail the influence of temperature nor the droplet size effects on the contact angle. Instead, we only aim at illustrating the link between our model fluid and realistic liquids. We applied a constant temperature $T = 0.85\epsilon/k_B$ that we used in the mechano-caloric route, controlled by a Nosé-Hoover thermostat. The amount of fluid particles is $\sim$ 12 000, enclosed by two solid walls located in the x, y-plane. Periodic boundary conditions apply in the directions parallel to the walls. As mentioned above, the cut-off radius in this work is relatively longer than that used traditionally, and we have carefully chosen the simulation box size such that the liquid has sufficient space in all dimensions. We ran firstly an equilibration period of 10 000 time steps, followed by 1 million time steps of production.

The density profile was sampled via binning in a slab system along the normal direction to the wall. The contact angle of the sessile droplet was estimated by fitting the apparent density profile with a spherical shape, given by the following equation:

$$\rho_{\rm app}(z) = \frac{(\rho_l - \rho_v)\pi r(z)^2}{L_x L_y} + \rho_v, \tag{S23}$$

where $\rho_{\rm app}$ is the apparent density representing the ratio of liquid molecules number in a slab and the slab volume, ρ_l and ρ_v are the real liquid and vapor densities, respectively, and r is the radius of the droplet section in the target slab. Since $r(z)$ is a function of the radius R and the center position z_0 of the sphere ($r(z)^2 = R^2 - (z - z_0)^2$), by fitting the curve, one can

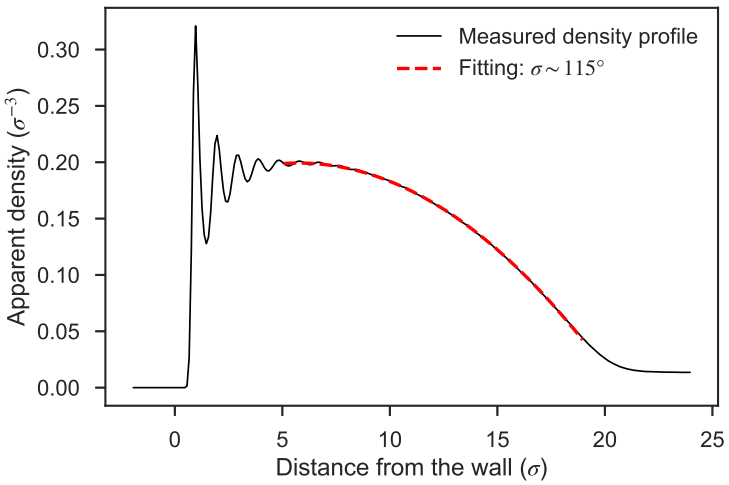

FIG. S11. Apparent density profile of a sessile droplet with $\epsilon_{ls} = 0.4$ at $T = 0.85\epsilon/k_B$. Fitting the data with Eq. S23 reveals $\theta \sim 112°$.

deduce $\theta = \arccos(-z_0/R)$. An example is shown in fig. S11. Figure S12 shows the evolution of contact angles θ as a function of interaction energy ϵ and the corresponding value of $\cos\theta$. The uncertainty for each measurement of θ was estimated to be approximately 2°, which is omitted for clarity. For $0.2 \leq \epsilon \leq 0.8$, the contact angle varies from 156° to 25°. Drying is observed when $\epsilon = 0.1$, and the curve of $\cos\theta$ suggests a continuous drying transition. This has been discussed in Ref [S15], which elucidates that using a short-ranged interaction potential can yield a shift of drying transition to a nonzero value of ϵ. On the other hand, wetting is found when $\epsilon \geq 0.9$.

VI. CONTACT ANGLE AND SLIP LENGTH IN WATER-GRAPHENE SYSTEMS

For the purpose of better knowing our water-graphene system, we conducted similar simulations as described above for the LJ system to measure the contact angle θ. Meanwhile, another equilibrium molecular simulation was performed to compute the slip length b.

In terms of contact angle measurement, the initial configuration was set as described by Wang et al.[S16]. The system contains 1000 water molecules, a graphene film with the dimensions of 115.6 Å in length and 106.5 Å in width. All the force fields are identical to those we presented in section I B. A Nosé-Hoover thermostat was applied to control the tem-

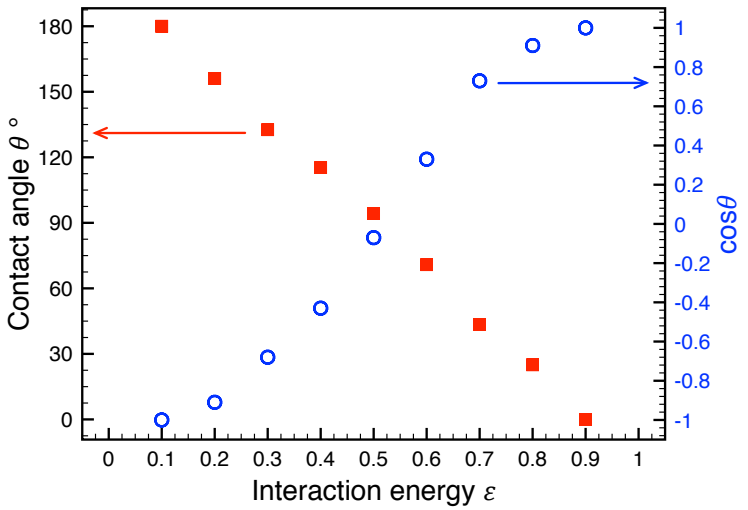

FIG. S12. Red full squares: contact angle θ as a function of the interaction energy at temperature of $T = 0.85\epsilon/k_B$. The incertitude is not shown but is approximately 2° for each point. Blue open circle: the corresponding value of $\cos\theta$.

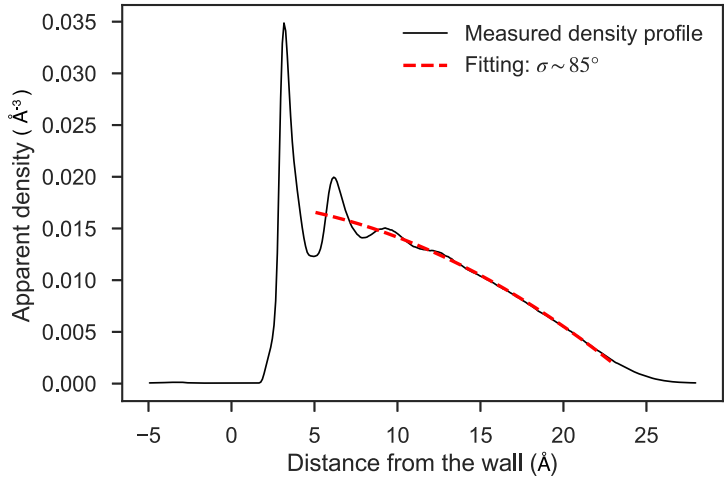

FIG. S13. Apparent density profile of a sessile droplet of water on a graphene film. Fitting the data with Eq. S23 provides $\theta \sim 85°$.

perature at 323 K. Periodic boundary conditions are used in the x and y directions, whereas a simple non-periodic boundary condition is applied on the z-axis. After an equilibration period of 500 ps, we ran the production for another 500 ps. The contact angle was evaluated by fitting the apparent density profile $\rho_{app}(z)$.

In figure S13 we plot the apparent density profile of the water-graphene system. The contact angle is revealed to be $85° \pm 1°$. In Ref. [S16], Wang et al. reported a contact angle of 93.9° in their MD simulations at the same temperature. Knowing that the real value of the contact angle of water on an isolated graphene monolayer remains unknown but around 90°, and the contact angle changes significantly as a function of the water-carbon interaction energy (indeed we used a different force field than that used by Wang et al.), the results seem reasonnable.

For the slip length measurement, we used the relation between the slip length b and the interfacial friction coefficient λ: $b = \eta/\lambda$, as indicated in the main text. The interfacial friction coefficient was expressed via linear response theory in terms of a Green-Kubo relationship, which relates the friction coefficient λ to equilibrium fluctuations of the friction force [S17, S18]:

$$\lambda = \lim_{t\to\infty} \lambda_{GK}(t), \tag{S24}$$

with

$$\lambda_{GK}(t) = \frac{1}{Ak_BT} \int_0^t \mathrm{d}t \langle F_i(t)F_i(0)\rangle_{equ}, \tag{S25}$$

where A is the contact area, $F_i(t)$ is the total tangential force acting along the $i = x, y$ direction.

In this study, we built a graphene sheet with dimensions of $L_x = 25.56$ Å and $L_y = 24.60$ Å, above which 392 water molecules were added. The dimensions of the simulation box are determined by the graphene sheet in the x and y directions, while the box height in the z direction was set to be 50 Å, so as to leave a large gap between the periodic images of the system in the z direction. Periodic boundary conditions apply in all directions. Temperature was controlled by a Nosé-Hoover thermostat at 323 K. After 100 ps for equilibration, the production run lasted another 100 ps.

Time autocorrelation of forces in both x and y directions were recorded. Figure S14 plots the evolution of λ_{GK} as a function of time. The friction coefficient λ is given by the plateau value yielding 1.7×10^4 N s/m^3 for our system, which is of the same order of magnitude as that reported by Kannam et al. [S19] (1.25 ± 0.10 10^4 N s/m^3, using equilibrium molecular simulations). The viscosity of TIP4P/2005 water at 323 K is well documented in the literature [S20–S22], whose value is estimated to be ~ 0.55 mPa.s. Using the relation $b = \eta/\lambda$, we obtain the slip length of water on the graphene surface $b \approx 32$ nm.

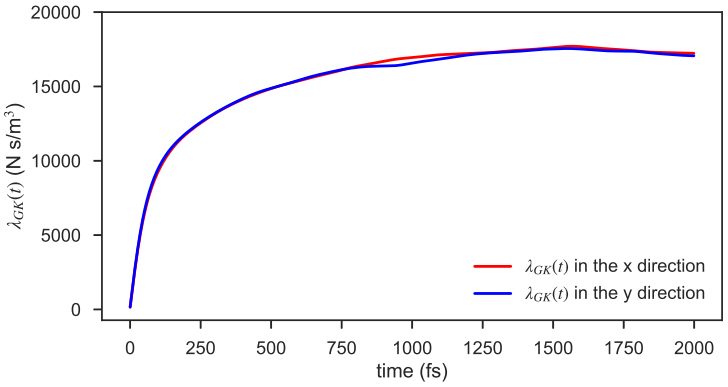

FIG. S14. Green-Kubo estimate of the interfacial friction coefficient.The friction coefficient λ is given by the plateau value of $\lambda_{GK}(t)$ at long times: $\lambda \approx 1.7 \times 10^4$ N s/m^3.

Ref. [S23] reviews the slip length of water in CNTs of diameter from 0.81 to 10 nm and that of water on a planar graphene surface. The results range from 1 to ca. 100 nm. Our value is therefore reasonable in order of magnitude.

VII. CHARACTERISTIC LENGTH *L*

In order to interpret the massive enhancement of M_{21} at low ε_{ls}, we introduce a characteristic length L representative of the extension of the region where the enthalpy differs from the bulk. Let's consider firstly a no-slip hydrodynamic boundary condition, the thermo-osmosis coefficient is expressed by :

$$M_{12}^{\mathrm{no-slip}} = M_{21}^{\mathrm{no-slip}} = \frac{1}{\eta}\int_{z_s}^{+\infty} (z - z_s)\,\delta h(z)\,\mathrm{d}z, \tag{S26}$$

with η the liquid viscosity, z_s the shear plane position and $\delta h(z)$ the excess specific enthalpy.

Now we consider the slip length b at the interface, we have a modified formula:

$$M_{12} = M_{21} = \frac{1}{\eta}\int_{z_s}^{+\infty} (z - z_s + b)\,\delta h(z)\,\mathrm{d}z. \tag{S27}$$

We would like to emphasize the crucial role of the slip length b, so we compare these two expressions:

$$\frac{M_{21}}{M_{21}^{\mathrm{no-slip}}} = \frac{\frac{1}{\eta}\int_{z_s}^{+\infty}(z - z_s + b)\,\delta h(z)\,\mathrm{d}z}{\frac{1}{\eta}\int_{z_s}^{+\infty}(z - z_s)\,\delta h(z)\,\mathrm{d}z} = 1 + \frac{b\int_{z_s}^{+\infty}\delta h(z)\,\mathrm{d}z}{\int_{z_s}^{+\infty}(z - z_s)\delta h(z)\,\mathrm{d}z}. \tag{S28}$$

We can then rewrite the expression for the thermo-osmosis coefficient in the presence of slip as:

$$M_{21} = M_{21}^{\mathrm{no-slip}}(1 + b/L), \tag{S29}$$

with

$$L = \frac{\int_{z_s}^{+\infty}(z - z_s)\delta h(z)\ \mathrm{d}z}{\int_{z_s}^{+\infty}\delta h(z)\ \mathrm{d}z}. \tag{S30}$$

VIII. BACKFLOW VELOCITY ANALYSIS

Viscous dissipation at the entrances of the nanochannel due to the focusing of the streamlines generates pressure drops at the entrances. Since the pressure is the same in both reservoirs, this induces a pressure gradient along the nanochannel. A Poiseuille backflow is then be created and one can deduce its velocity profile $v_{bk}(z)$ from the measured curvature of the velocity profile, using the same method presented in Section I via Eq. S3.

From the pressure gradient generating the backflow, we calculate a characteristic term of $\nabla P/(\eta\nabla T/T_{avg})$, where ∇P is the pressure gradient, η is the liquid viscosity, ∇T and T_{avg} are respectively the temperature gradient and the average temperature.

This term depends only on ε_{ls}. Since we assume that the measured velocity v_m is the result of linear addition of that for thermo-osmotic flow and for pressure induced backflow, the backflow's velocity can be determined as $v_{bk} = v_m - v_s$. Knowing that v_{bk} has a negative sign against v_m and v_s, one can write

$$v_{bk} = v_s - v_m = (M_{\mathrm{real}} - M_{\mathrm{m}})\nabla T/T_{\mathrm{avg}}. \tag{S31}$$

On the other hand, the backflow is induced by entrance effects and its velocity v_{bk} is proportional to $(\nabla P/\eta)$ with a prefactor A, which depends on the geometry of the slit and on the slip length. Equation S31 can be rewritten as

$$\frac{\nabla P}{\eta\nabla T/T_{\mathrm{avg}}} = \frac{M_{\mathrm{real}} - M_{\mathrm{m}}}{A}. \tag{S32}$$

Using the same geometry for all the simulations in the mechano-caloric configuration, the right side of Eq. S32 relies only on ε_{ls}, and the term $\nabla P/(\eta\nabla T/T_{\mathrm{avg}})$ can be used for characterizing the backflow induced by entrance effects.

[S1] S. Plimpton, J. Comput. Phys. **117**, 1 (1995).

[S2] A. I. Jewett, Z. Zhuang, and J.-E. Shea, Biophys J **104**, 169a (2013).

[S3] W. Humphrey, A. Dalke, and K. Schulten, Journal of molecular graphics **14**, 3338 (1996).

[S4] G. Bussi, D. Donadio, and M. Parrinello, J. Chem. Phys. **126**, 014101 (2007).

[S5] J.-L. Barrat and L. Bocquet, Physical Review Letters **82**, 46714674 (1999).

[S6] `http://lammps.sandia.gov/doc/compute_stress_atom.html`.

[S7] J. L. F. Abascal and C. Vega, The Journal of Chemical Physics **123**, 234505 (2005).

[S8] J. H. Los and A. Fasolino, Physical Review B **68**, 024107 (2003).

[S9] G. Pérez-Hernández and B. Schmidt, Physical Chemistry Chemical Physics **15**, 4995 (2013).

[S10] Y. S. Al-Hamdani, D. Alfè, and A. Michaelides, J. Chem. Phys. **146**, 094701 (2017).

[S11] A. P. Bregulla, A. Würger, K. Gnther, M. Mertig, and F. Cichos, Physical Review Letters **116**, 1883035 (2016).

[S12] D. Huang, C. Cottin-Bizonne, C. Ybert, and L. Bocquet, Phys. Rev. Lett. **98**, 177801 (2007).

[S13] D. M. Huang, C. Cottin-Bizonne, C. Ybert, and L. Bocquet, Langmuir **24**, 1442 (2008).

[S14] L. Bocquet and J.-L. Barrat, Soft Matter **3**, 685 (2007).

[S15] R. Evans, M. C. Stewart, and N. B. Wilding, Phys. Rev. Lett. **117**, 176102 (2016).

[S16] W. Wang, H. Zhang, S. Li, and Y. Zhan, Nanotechnology **27**, 075707 (2016).

[S17] G. Tocci, L. Joly, and A. Michaelides, Nano Lett. **14**, 6872 (2014).

[S18] K. Falk, F. Sedlmeier, L. Joly, R. R. Netz, and L. Bocquet, Nano Lett. **10**, 4067 (2010).

[S19] S. Kumar Kannam, B. D. Todd, J. S. Hansen, and P. J. Daivis, J. Chem. Phys. **136**, 024705 (2012).

[S20] G. Guevara-Carrion, J. Vrabec, and H. Hasse, J. Chem. Phys. **134**, 074508 (2011).

[S21] E. Guillaud, S. Merabia, D. de Ligny, and L. Joly, Physical Chemistry Chemical Physics **19**, 2124 (2017).

[S22] a. P. Markesteijn, R. Hartkamp, S. Luding, and J. Westerweel, J. Chem. Phys. **136**, 134104 (2012).

[S23] S. K. Kannam, B. D. Todd, J. S. Hansen, and P. J. Daivis, J. Chem. Phys. **138**, 094701 (2013).